Model analysis and electrical characterization of atmospheric pressure cold plasma jet in pin electrode configuration

G. Divya Deepak,[1,a] N. K. Joshi,[1] and Ram Prakash[2]

[1]*Department of Nuclear Science and Technology, Mody University of Science and Technology, Lakshmangarh (Sikar) 332311, India*
[2]*Plasma Devices Laboratory, CSIR-Central Electronics Engineering Research Institute, Pilani 333031, India*

In this study, both model analysis and electrical characterization of a dielectric barrier discharge based argon plasma jet have been carried at atmospheric pressure in a pin electrode configuration. The plasma and fluid dynamics modules of COMSOL multi-physics code have been used for the modeling of the plasma jet. The plasma parameters, such as, electron density, electron temperature and electrical potential have been analyzed with respect to the electrical parameters, i.e., supply voltage and supply frequency with and without the flow of gas. In all the experiments, gas flow rate has been kept constant at 1 liter per minute. This electrode configuration is subjected to a range of supply frequencies (10-25 kHz) and supply voltages (3.5-6.5 kV). The power consumed by the device has been estimated at different applied combinations (supply voltage & frequency) for optimum power consumption at maximum jet length. The maximum power consumed by the device in this configuration for maximum jet length of ~26 mm is just ~1 W. © *2018 Author(s). All article content, except where otherwise noted, is licensed under a Creative Commons Attribution (CC BY) license (http://creativecommons.org/licenses/by/4.0/).* https://doi.org/10.1063/1.5023072

I. INTRODUCTION

Atmospheric pressure plasma jets (APPJs) offer a chamberless delivery of downstream reaction, ideal for many areas, such as, material surface treatment, nano-structure fabrication, sterilization, disinfection, biomedicine, etc.[1–12] Atmospheric pressure cold plasma jets operating with noble gasses can be classified into four categories, i.e., dielectric-free electrode (DFE) jets, dielectric barrier discharge (DBD) jets, DBD-like jets and single electrode (SE) jets.[13–16]

Raizer[17] had discussed the basic discharge mechanism of DBD plasmas. It is shown that for air gaps created by the plane electrodes the Townsend mechanism of avalanche multiplication is employed if p.d<200 Torr.cm and for p.d>5000 Torr.cm, steamer breakdown is employed. Here p is the pressure and d is the distance between the electrodes. Streamer type of breakdown is typical for relatively large air gaps. Since p.d<200 Torr.cm for the pin electrode configuration described in this paper, so the discharge mechanism is predominantly governed by Townsend breakdown mechanism which is associated with the development of multiple avalanches. The pin electrode configuration in this paper has been developed to optimize the operating parameters (supply voltage, supply frequency) to generate cold plasma jet with longer jet lengths that could be employed for biomedical applications. The pin electrode based APPJ device presented in this paper satisfies all the necessary conditions for its applications in plasma medicine, which are no risk[1] of arcing, jet ejecting in air, low gas temperature and rich active species.

Liu and Neiger[18] (2003) proposed an electrical model of a DBD for arbitrary excitation voltage.

---

[a]G Divya Deepak (Corresponding author) Email- divyadeepak77@gmail.com

M. Teschke et al.[19] (2005) investigated the propagation of an atmospheric pressure plasma jet (APPJ) is investigated by use of an intensified charge coupled device (ICCD) camera. It is shown that the APPJ is mainly an electrical phenomenon and not a flow related one. This device consumed a maximum power of 4 W whereas the electrode configuration described in this research paper consumes only ~1 W. XinPei Lu and Mounir Laroussi[20] (2006) studied dynamics of APPJ generated by submicro second pulses using V-I characteristics and also used CCD camera for investigating the temporal and spatial evolutions of the plasma inside the discharge chamber.

Yong and Han[21] (2006) generated nitrogen based micro plasma jet at atmospheric pressure using two aluminum disks in which the measured gas temperature was less than $300\,^{0}K$ and it was proposed to be used for biomedical applications. XinPei Lu et al.[22] (2008) generated a cold plasma jet of 11 cm using a kHz ac power supply for biomedical applications but did not perform the comprehensive electrical characterization of the device. Qiu-Yue Nie et al.[23] (2008) generated an argon based plasma jet using a pair of tungsten pin electrode which were separated by 2.5 mm. One of these tungsten pin electrodes was at floating potential. The effect of the flow velocity and applied potential on plasma jet was analyzed but power consumption by plasma jet was not calculated. U. Pal et al.[24] (2012) made an effort to understand multiple-peak discharge phenomenon based on an equivalent circuit model. Radu et al.[25] studied atmospheric glow discharge in dielectric barrier discharge reactor under varying experimental conditions (frequency, gap length, & electric field intensity) which enabled them to characterize DBD's electrically.

Hyun Kim[26] et al. (2009) generated argon based plasma using a piezo transformer which consumed a peak power of 2 W. HONG Yi[27] et al. (2013) succeeded in generating a DBD argon based plasma jet using screw ring-ring electrodes, where the optical emission spectra of argon have been analysed to find out the discharge parameters, such as, gas temperature and power consumed with respect to the supply voltage and frequency. Hea Min Joh[28] et al. (2014) successfully generated a helium based plasma jet using pin electrode configuration where the effects of electrode materials, a ground ring electrode, and nozzle shape on the plasma was studied but did not provide details about the power consumed by the device at different supply voltages and frequencies. A. Shashurin et al.[29] (2015) reviews recent research efforts undertaken in the area of non-equilibrium atmospheric plasma jets with special focus on experimental approaches.

Electrical characterization of a ring electrode based atmospheric pressure DBD cold plasma has been carried out with consumed power details by G Divya Deepak et al. (2016).[30] The effect of floating electrodes on formation of atmospheric plasma jet has also been analysed by G Divya Deepak et al. (2017).[31]

Kelly & Turner[32] (2011) developed the fluid model of 2D cross-section of an AC driven plasma at atmospheric pressure using COMSOL. In 2006 Tendero et al.[33] successfully modeled DBD reactor with a flow of air using COMSOL and in the same year Sakiyama & Graves[34] worked on modeling of RF (13.56 MHz) plasma needles based on a fluid model having Helium and a small fraction of nitrogen. Initial work in modeling of DBD was only done for the static discharge of gas and only a few studies have been performed to model DBD based APPJ's incorporating the flow of gas. Modelling of streamer like APPJ was done by G. V. Naidis[35] in 2012. In 2013 Siddharth et al[36] developed a fluid model for a partially packed dielectric barrier discharge plasma reactor employing pure He using COMSOL multiphysics.

In this work, an effort has been made to model DBD-APPJ in pin electrode configuration by incorporating flow of gas using fluid dynamics module of COMSOL 5.2a (i.e., multi-physics code). Model results are compared with the electrical characterization of the developed cold plasma jet source. Since electrical characterization of an electrode configuration is imperative in establishment of optimized operating range, therefore, the power consumed by the device along with jet length (with & without sleeve) at various supply voltages and frequencies have been analysed in depth.

II. GEOMETRY AND EXPERIMENTAL SETUP

The geometrical details for the plasma jet generation using pin electrode configuration is shown in Fig. 1 whereas its experimental setup in two configurations, i.e., without quartz sleeve and with
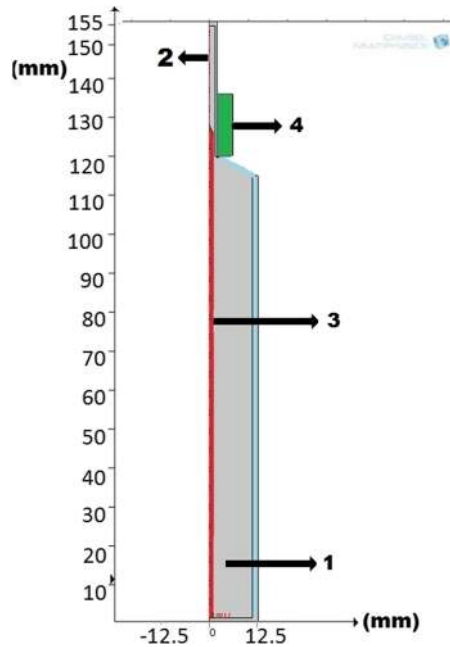
FIG. 1. Geometry of pin electrode configuration.

quartz sleeve (indicated by green colour) are shown in Fig. 2. The main body of the jet consists of a quartz tube of length and inner diameter 155 mm and 22 mm, respectively, which serves as a dielectric barrier between the electrodes. The argon gas flows through the inlet of the quartz tube whose inner diameter is 22 mm and outer diameter 25 mm indicated as 1 in the geometrical design (see Fig. 1). The thickness of the quartz tube is 1.5 mm. There is a central pin electrode made of copper (indicated as 3) of length 128 mm and thickness 2 mm runs through the quartz tube that acts as the powered electrode. The nozzle outlet is indicated by 2 whose inner diameter is 3 mm and outer diameter is 6 mm. Further, the total length of the nozzle is 35 mm. A ring electrode (grounded) (indicated as 3) of length 15 mm and thickness 4 mm is wound on top of the nozzle(see Fig. 1). Hence, the effective length of nozzle is only 20 mm after accounting for the ring electrode. The pin
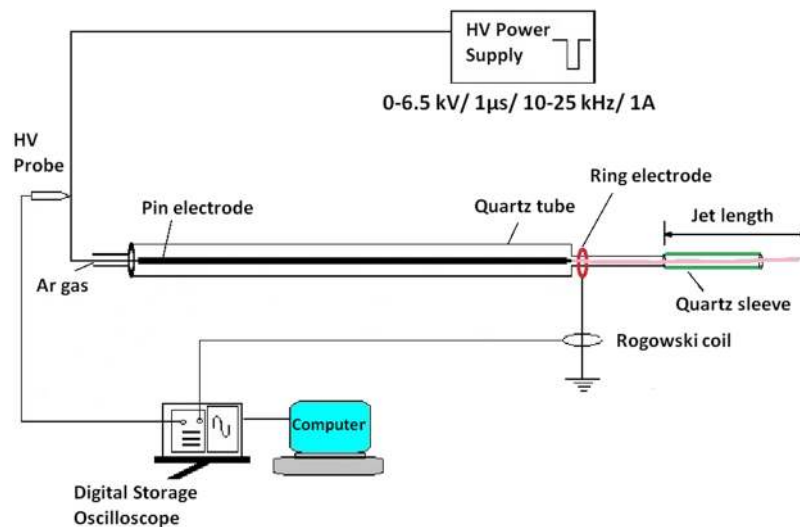

FIG. 2. Experimental set up of atmospheric pressure plasma jet using pin electrode configuration (with quartz sleeve).

FIG. 3. Cold Plasma jet generated using pin electrode configuration.

electrode and ring electrode are separated by a distance of 2 mm that includes the thickness of quartz tube (1.5mm) and the gap between the pin electrode and the inner wall of the quartz tube (0.5 mm). In the other set of experiments a quartz sleeve of inner diameter 7 mm, outer diameter 10 mm and 15 mm length was placed on the nozzle of the quartz tube (see Fig. 2) to observe the variation in the length of plasma jet. The applied voltage and currents are measured by using a high voltage probe (Tektronix P 6015 A) (Bandwidth 0-75 MHz) and Rogowski-type Pearson current monitor (Model 110) (0.1VA−1, 1Hz–20 MHz, 20 ns usable rise time) connected to a digital storage oscilloscope (Tektronix DPO 4054, bandwidth: 500 MHz).

The experiments have been performed using argon gas with a flow rate of 1 lit/min in an airtight arrangement at atmospheric pressure. A typical cold plasma jet generated using pin electrode configuration is shown in Fig. 3.

III. MODEL ANALYSIS

In this work the fluid dynamics module of COMSOL 5.2a has been used, which is based on Finite Element Method. Using this module one can perform 1D, 2D and 3D modeling, and accordingly, simulation of plasma jets using various electrode configurations is possible. For each module, there are a set of domain equations that are specified to characterize the physics behind the processes involved. The physics interfaces include necessary tools to model plasma discharges, beginning with Boltzmann equation and two-term approximation solver that computes the electron transport properties and source coefficients from a set of electron impact collision cross sections.[37]

A. Governing equations for discharge simulations

The electron density and mean electron energy are computed by solving the following pair of drift-diffusion equations for the electron density and mean electron energy.

$$\partial/\partial t(n_e) + \nabla[-n_e(\mu_e E) - D_e \nabla n_e] = R_e \tag{1}$$

$$\partial/\partial t(n_\varepsilon) + \nabla[-n_\varepsilon(\mu_\varepsilon E) - D_\varepsilon \nabla n_\varepsilon] + E\Gamma_e = R_\varepsilon \tag{2}$$

$$\Gamma_e = -(\mu_e E)n_e - D_e \nabla n_e \tag{3}$$

Here n_e is the electron density, n_ε is the electron energy density, μ_e is electron mobility, μ_ε is the electron energy mobility, E is electric field, R_e is the electron rate expression, R_ε is the energy loss/gain due to inelastic collisions, D_e is Diffusion coefficient of electrons, D_ε is electron energy diffusivity, Γ_e is electron flux.

The source coefficients in the above equations are determined by the plasma chemistry using rate coefficients. In case of rate coefficients, the electron source term is given by,

$$R_e = \sum_{j=1}^{M} x_j k_j N_n n_e \tag{4}$$

where x_j is the mole fraction of the target species for reaction j, k_j is the rate coefficient for reaction j and N_n is the total neutral number density. The electron energy loss is obtained by summing the collisional energy loss over all reactions and is expressed as,

$$R_\varepsilon = \sum_{j=1}^{P} x_j k_j N_n n_e \Delta\varepsilon_j \tag{5}$$

where $\Delta\varepsilon_j$ is the energy loss from reaction j. The rate coefficients can be computed from cross section data by the following integral,

$$k_k = \gamma \int_0^\infty \varepsilon \sigma_k(\varepsilon) f(\varepsilon) d\varepsilon \tag{6}$$

where $\gamma = (2q/m_e)^{1/2}$, m_e is the electron mass, ε is the energy (SI unit: Joule), σ_k is the collision cross section, and f is the electron energy distribution function. In this case, the electron energy distribution function (EEDF) is assumed Maxwellian because in DBD plasmas the degree of ionization is high and as a consequence, the electron-electron collisions drive the distribution towards Maxwellian shape.

The EEDF can be computed by solving the Boltzmann equation. The evolution of the distribution function, f, in a six-dimensional phase space is expressed as,

$$\partial f / \partial t + v\nabla f - (eE/m)\nabla_v f = C[f] \tag{7}$$

where f is the electron distribution function, v is the velocity coordinate, e is the elementary charge, m is the electron mass, E is the electric field, ∇_v is the velocity-gradient operator and C represents the rate of change in f due to collisions.

In the code, EEDF is assumed to be almost spherically symmetric, so the series can be truncated after the second term (a so-called two-term approximation). An anisotropic perturbation is also applied due to inelastic collisions under consideration. The detailed explanation of two-term approximation is given elsewhere.[37]

The electron diffusivity, energy mobility, and energy diffusivity can be computed from the electron mobility using the following relationship,

$$D_e = \mu_e T_e, \ \mu_\varepsilon = (5/3)\mu_e, \ D_\varepsilon = \mu_\varepsilon T_e \tag{8}$$

where T_e is the temperature of the electron,

$$\text{mean electron energy,} \quad \bar{\varepsilon} = \frac{n_\varepsilon}{n_e} \tag{9}$$

$$\text{electron temperature,} \quad T_e = (\frac{2}{3})\bar{\varepsilon} \tag{10}$$

B. Governing equations of fluid dynamics module

Governing equations describing the fluid theory originated by solving a set of moments of the Boltzmann equation. Typically, for most applications, the first three moments are considered, which describe the particle, momentum, and energy conservation. By taking these moments, the Boltzmann equation is reduced to a 3-dimensional, time dependent problem and describes the plasma in terms of averaged quantities such as density, momentum, and mean energy. The coupling of flow equations and plasma occurs through temperature field. The zeroth moment of the Boltzmann equation gives the continuity equation describing the rate of change of particles (electrons, ions, or neutral species).[35,38,39]

$$\frac{\partial}{\partial t}\left(n_p\right) + \nabla\Gamma_p = R_p \tag{11}$$

The subscript p refers to different species such as electrons, ions or neutral species, n represents the density of species, Γ represents the flux vector, and R_p represents either the source/sink term and accounts for the production or loss of a particular species p in chemical reactions, ionization events, etc.

Losses at the wall are accounted in the boundary conditions and are not explicitly considered in the particle continuity equations.

Flux term for the particles (based on drift-diffusion approximation) consists of a diffusion term and a drift term given as,

$$\Gamma_p = \pm n_p \mu_p E - D_p \nabla n_p \tag{12}$$

where E refers to the electric field, μ and D refer to the mobility and diffusion coefficient of the species. The first term of the equation 12 is zero for the neutral species.

The source/sink term, R_p is calculated as

$$R_p = \sum \left(c_{pj} \, r_{pj} \right) \tag{13}$$

where c_p represents stoichiometric coefficient and r_p represents the reaction rate of the target species for reaction j.

The second moment of the Boltzmann equation is used to derive the energy conservation equation. The final expression for rate of change of electron energy density including the drift diffusion approximation is described as

$$\frac{\partial}{\partial t}(n_\varepsilon) + \nabla \Gamma_\varepsilon + E\Gamma_e = R_\varepsilon \tag{14}$$

where n_ε is the electron energy density, and R_ε is the energy loss/gain due to inelastic collisions. The flux vector for electron energy Γ_ε is given as

$$\Gamma_\varepsilon = -\frac{5}{3}(\mu_e E)n_\varepsilon - \frac{5}{3}\nabla D_e n_\varepsilon \tag{15}$$

A self consistent electric field distribution is calculated by solving the Poisson's equation in the plasma region and the Laplace's equation in the dielectric material.

$$-\nabla \varepsilon_0 \varepsilon_r \nabla V = \rho \tag{16}$$

$$-\nabla^2 V = 0 \tag{17}$$

$$E = -\nabla V \tag{18}$$

where ε_0 is the permittivity of free space, ε_r the relative permittivity, ρ is the space charge density (m^{-3}), and V is the applied potential.

The space charge density ρ is automatically computed based on the plasma chemistry specified in the model using the formula:

$$\rho = q\left[\sum_{k=1}^{N} z_k n_k - n_e\right] \tag{19}$$

Surface charge accumulation on the dielectric layer due to difference in fluxes between the electrons and ions is taken into account using the following boundary conditions:

$$-n(D_1 - D_2) = \rho_s \tag{20}$$

$$d\rho_s/dt = nJ_i + nJ_e \tag{21}$$

where n is the unit normal, ρ_s is the surface charge density, D_1 and D_2 are the electric displacement fields on both sides of the boundary, and J_i and J_e are the total ion and electron current densities at the wall. A set of 9 reactions involving argon atoms, ions and metastables have been used in this model.[40] The pin electrode configuration is subjected to applied voltage amplitude (3.5 kV to 6.5 kV) at a frequency range of (10-25 kHz). To begin the simulation seed electrons $\sim 10^9$ m^{-3} have been taken into account because any sample of gas under normal condition contains an average of 10^9 m^{-3} electrons and ions due to ultraviolet, cosmic radiations, radioactivity, etc.[17] So, an electron density $\sim 10^9$ m^{-3} is loaded uniformly in the electrode gap along with the argon gas to initiate the discharge at the room temperature. A unipolar pulse with pulse width 1μsec has been applied across the boundary

of the one of the electrode to initiate the discharge. All the operating conditions of the discharge are similar to the experimental conditions.

C. Boundary conditions

Electrons are lost to the wall due to random motion within a few mean free paths of the wall and gained due to secondary emission effects, resulting in the following boundary condition for the electron flux;

$$-n\Gamma_e = ((1/2)v_e)n_e - \sum_p \gamma_p(\Gamma_p n) \tag{22}$$

and electron energy flux is computed as

$$-n\Gamma_\varepsilon = ((5/6)v_e)n_\varepsilon - \sum_p \varepsilon_p\gamma_p(\Gamma_p n) \tag{23}$$

where v_e is the collision frequency. The second term on the right hand side of Equation (18) is the gain of electrons due to secondary emission effects, γ_p is the secondary emission coefficient. The second term in Equation (21) is the secondary emission energy flux, ε_p being the mean energy of the secondary electrons. At the walls, argon metastables quench and change back to neutral argon atoms. Argon ions also change back to neutral argon atoms while emitting secondary electrons. The electrical potential at the exterior boundary of the dielectric barrier discharge is 0 V. The discharge simulations for the pin electrode configuration have been carried out for both, the static mode and with the flow of argon gas. The gas flow rate is fixed at 1 liter per minute for all simulations. Discharge simulations for the pin electrode configuration are time dependent solutions performed between time scales of 10^{-9} s to 10^{-6} s in a 99 time steps. The simulation program stops at the instant of discharge initiation due to convergence of the iterative algorithm of electron energy distribution function. A snapshot of the meshing with mesh area (1608 mm^2) of pin electrode configuration done using finite element method (FEM) is shown in Fig. 4. It is imperative to note that boundary layer meshing on the plasma volume allows us to resolve separation of space charge. The snapshots presented in Fig. 5, 6, 8 and 9 only depict the values of electron density, electron temperature and electrical potential at the instant of discharge initiation only and cannot depict 2 or more order difference in parameter values in a single snapshot.[36,40]
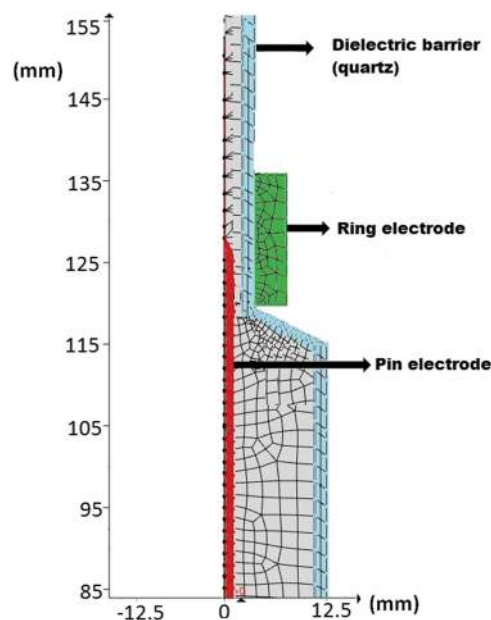

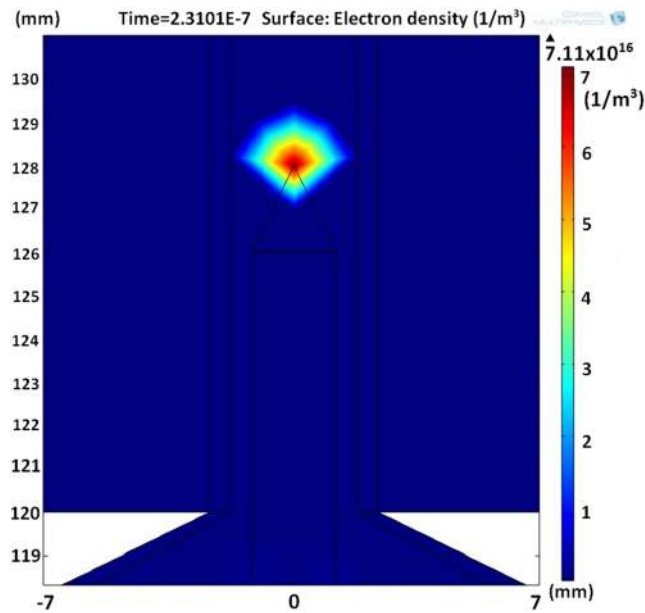FIG. 4. Meshing of pin electrode APPJ using Finite element method (FEM).

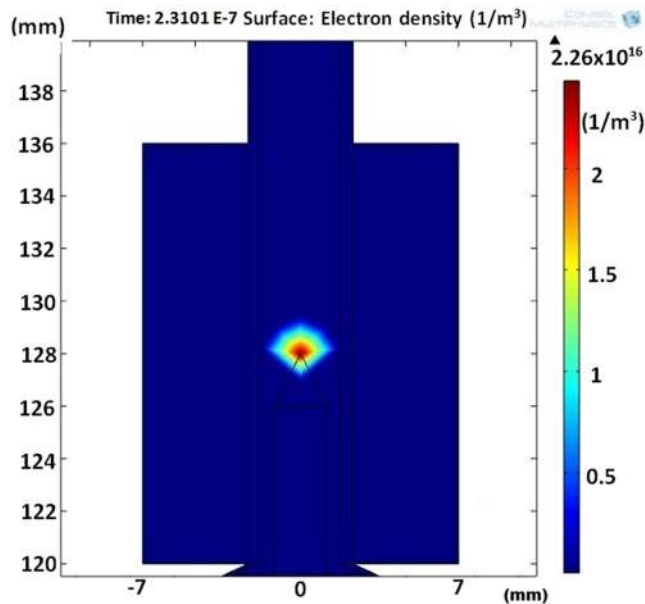FIG. 5. Electron density at 4.5 kV/25 kHz (static condition).

FIG. 6. Electron density at 4.5 kV/25 kHz (With flow).

IV. RESULTS AND DISCUSSION

A. Simulation analysis results

In the initial set of simulations, the supply voltage is kept constant at 4.5 kV and supply frequency is varied from 10-25 kHz to study its effect on plasma parameters. The spatial distribution of electron density at the moment of breakdown of Ar gas in static condition is shown in Fig. 5 and moment of breakdown with flow is shown in Fig. 6. It clearly shows that electron density is highest close to the pointed tip of the pin electrode due to the higher concentration of electric field. Fig. 7 depicts the variation of the electron density with respect to the change in supply frequency. It is inferred that
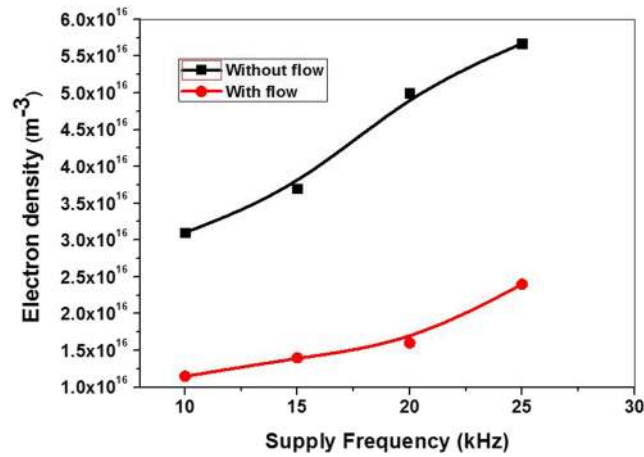
FIG. 7. Electron density Vs supply frequency at 4.5 kV.

there is an increase in electron density with increase in supply frequency for both, static mode and with flow of argon gas.

For all supply frequencies the electron density (without flow) is significantly higher than the electron density (with the flow) as the collisions between electrons and the argon atoms are more frequent in static mode.[16] It is interesting to note that the electron density rises significantly at higher supply frequency (25 kHz). This occurs because electrons have lesser transit time (i.e., ~ 40 μs) resulting in ion accumulation leading to more consumption of power by argon plasma jet.
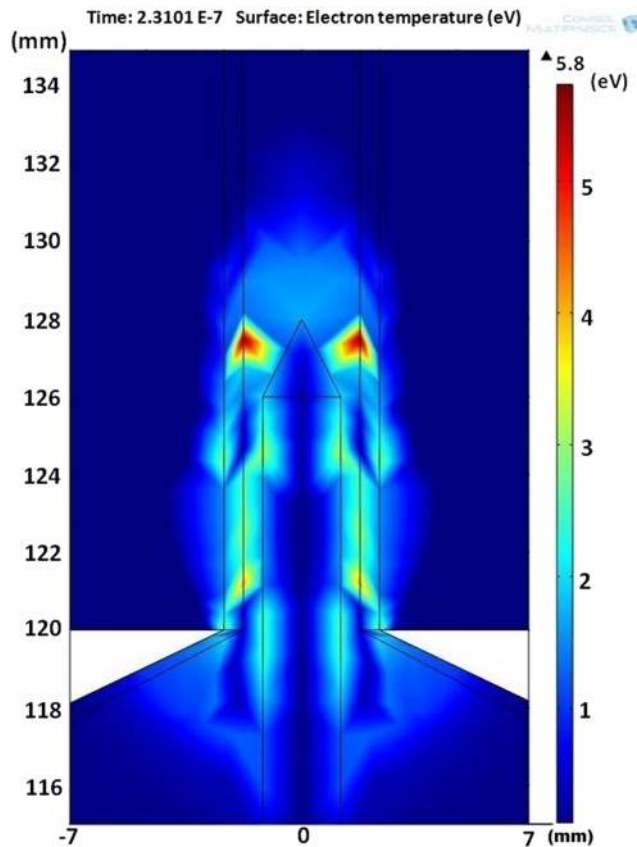
FIG. 8. Electron temperature at 4.5 kV/25 kHz (static condition).
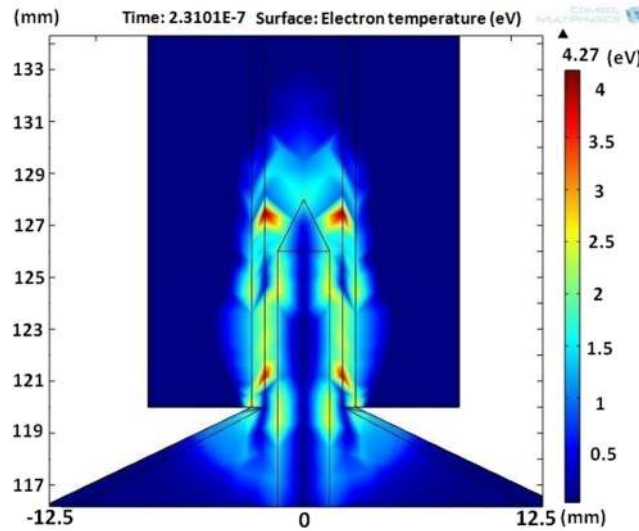
FIG. 9. Electron temperature at 4.5 kV/25 kHz (With flow).

This energy is absorbed by the seed electrons that are responsible for the secondary ionization of argon and hence resulting in avalanche process. Thereafter, there is an augmentation in electron density and perhaps expansion of luminous spots at cathode at higher supply frequencies is possible as reported elsewhere.[16] It is further seen from Fig. 7 that the electron density increases with supply frequency, this is because more energetic plasma electrons are present, which results in subsequent ionization of argon atoms and also can cause increased collisions between them and perhaps resulting in augmented energy exchange.

Fig. 8 & 9 depicts electron temperature distribution at the moment of breakdown of Ar gas in static condition and with flow at 4.5 kV/25 kHz. It illustrates the fact that electron temperature reaches maximum (4-6 eV) near the pointed tip of pin electrode indicating the highest concentration of electric field. Further, since the electron density is lesser in the condition of with flow of Ar gas compared to static condition hence the energy exchange between them is also less, thereby reducing the electron temperature. To show it more clearly a relationship between electron temperature and supply frequency for the developed pin electrode plasma jet is shown in Fig. 10. It again shows electron temperature increases with increase in supply frequency for both, the static and with the flow of argon gas. The electron temperature, being function of mean electron energy, it depends on the
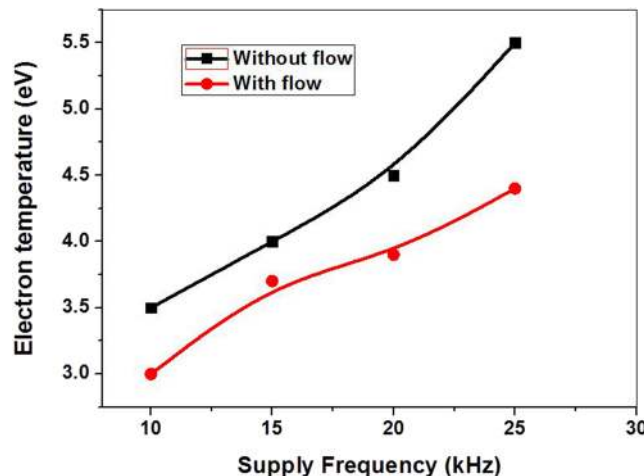

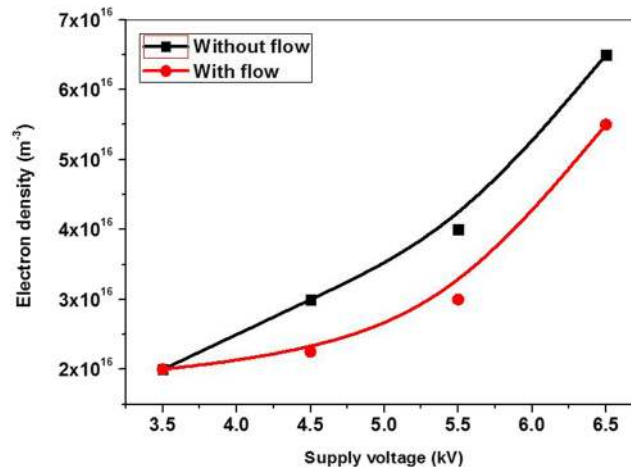FIG. 10. Electron temperature Vs supply frequency at 4.5 kV.

FIG. 11. Electron density Vs supply voltage at f=25 kHz.

electron density and electron energy density. As seen from Fig. 7, the electron density increases with supply frequency, more energetic electrons are present resulting in subsequent ionization of argon atoms, which causes increased collisions between electrons and results in more energy exchange between them. Consequently, the electron temperature also increases with the supply frequency for both static and with flow of argon gas.

A relationship between electron density and supply voltage is shown in Fig. 11. In this figure the supply frequency is fixed as 25 kHz and the electron densities have been compared at different applied voltages from 3.5 to 6.5 kV for both cases (static mode and with the flow of argon gas). It is evident that electron density increases with increase in supply voltage as more energetic electrons are available that cause electron avalanche. As seen earlier (from Fig. 7), the energetic electrons are available at higher supplied voltages, it results in higher ionization of argon atoms. At a lower voltage of 3.5 kV electron density in both cases remain at the same level because seed electrons present have not gained enough energy for secondary ionization, but at higher supply voltage (6.5 kV), the electron density in static mode is more compared with flow of argon gas due to more collisions between the electrons that occurs in the static mode.

Fig. 12 illustrates the relationship between electron temperature and supply voltage at 25 kHz. The electron temperature rises with higher applied potentials because at higher applied voltages the
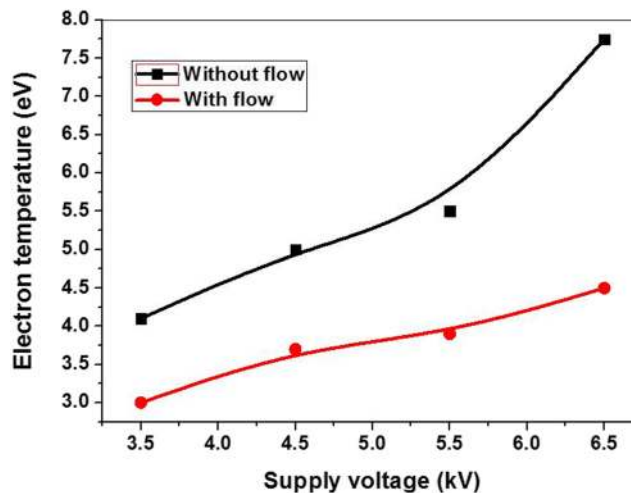

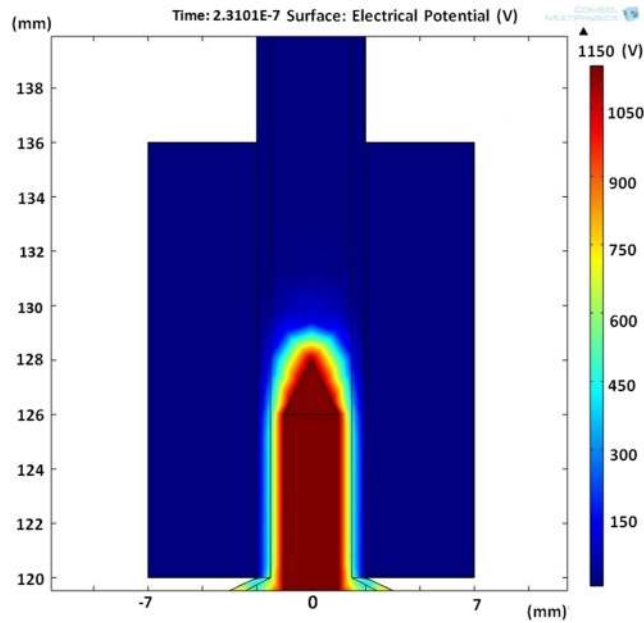FIG. 12. Electron temperature Vs supply voltage at f = 25kHz.

FIG. 13. Electrical potential reached at 4.5 kV/25 kHz (With flow).

seed electrons will absorb more energy and can result in energetic electrons collision with argon atoms further leading excitation and/or ionization. Moreover, as the collision process between the electrons becomes prominent in the static mode compared to the flow of argon gas, the electron temperature becomes higher for static mode for all supply voltages (see Fig. 11).

The electrical potential depicted in Fig. 13 & Fig. 14 is around 1.1 kV which appears to be quite lower than the experimental conditions. The simulated plasma potential in COMSOL multiphysics stops at the moment of breakdown of Argon gas (ie. discharge initiation) due to its iterative algorithm, hence it is not able to reach the electrical potential of the experimental condition. However, it can
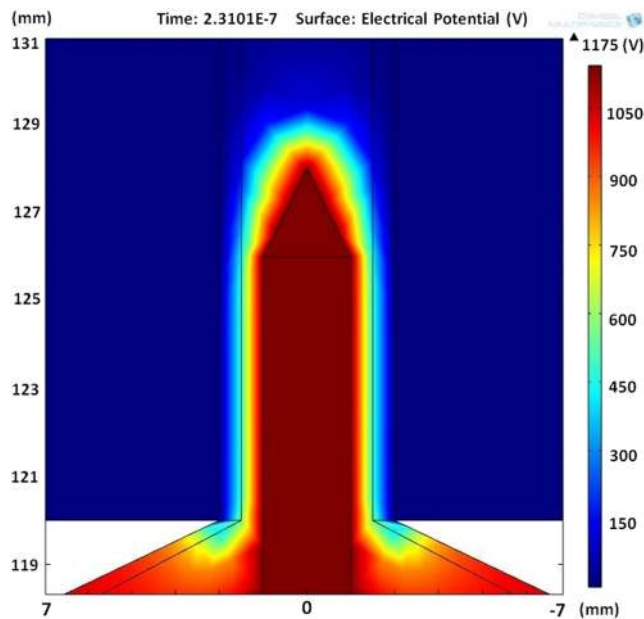

FIG. 14. Electrical potential reached at 4.5 kV/25 kHz (static condition).

be clearly seen Fig. 16 (experimental V-I characteristics at 4.5 kV/25 kHz) that discharge initiation occurs at around 1.1 kV where the discharge current starts flowing. This result is exactly matching with the simulation result of electrical potential withflow of Argon gas in Fig. 13 that stops at 1.1 kV. Furthermore, the corresponding electron density withflow of Argon gas is 2.26×10^{16} $(1/m^3)$ (see Fig. 6) which indicates the initiation of discharge. Hence our simulation results are in agreement with the experimental results.

The electrical potential proceeding from pointed tip of pin electrode towards the ring electrode at 4.5 kV/25 kHz in with flow of Ar gas and static condition is depicted in Fig. 13 & 14. It implicitly indicates that electric field strength is highest near the pointed tip of the pin electrode.

The relationship between electrical potential and supply frequency at fixed applied voltage 4.5 kV is illustrated in Fig. 15. It is quite evident that at lower supply frequencies the electrical potential reached for initiation of discharge is at the same level for both static mode and with flow of gas. Therefore, at 10 kHz, the electrical potential needed for initiation of discharge is almost at the same voltage level for both static modes and with the flow of argon gas. At these lower supply frequencies the electrons will also have a larger transit time of ~100 μs. However, at higher supply frequencies (20-25 kHz) the electrical potential reached for initiation of discharge is more prominent due to ion accumulation as electrons are having lesser transit time ~40 μs, which may result in more consumption of power.

B. Experimental results

A typical V-I characteristics of the developed APPJ using pin electrode at 4.5 kV, 25kHz with corresponding peak discharge current of 192 mA is shown in Fig. 16. In this paper the term power refers only to the power consumed by the device in W, which is obtained as a product of energy per pulse (Joules) and supply frequency (kHz). A digital storage oscilloscope (DSO) is used to record waveforms for each pulse of voltage and corresponding discharge current. These instantaneous values are multiplied (voltage & discharge current) and integrated over the duration of the pulse to obtain the energy consumed per pulse in Joules for a particular combination of supply voltage and frequency.[31,41] This energy per pulse is multiplied with the supply frequency to obtain the power consumed by the device in W. The energy consumed per pulse (in joules) at 4.5 kV/25 kHz (see Fig. 16) was found to be 2.08×10^{-5} Joules. Accordingly the power consumed by the device at 4.5 kV/25 kHz has been calculated by multiplying the energy consumed per pulse with the applied frequency(25 kHz), which yields the power consumed by the device at 4.5 kV/25 kHz as 0.52 W (see Fig. 17). Studies have been performed in order to understand the optimum range of operation for successful generation of cold plasma jet. We have used a unipolar square wave form voltage of 1 μs duration, where we do not have a smooth flat top region. It is well-known that in the dielectric
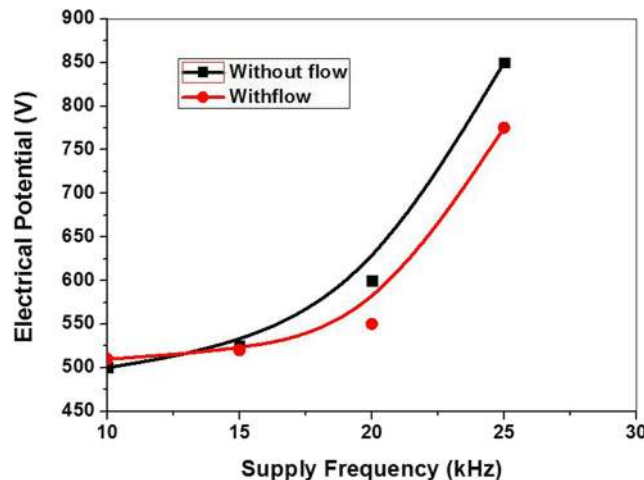

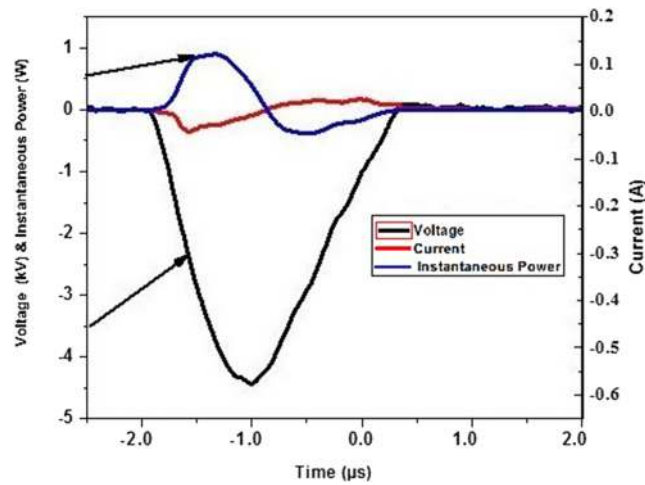FIG. 15. Electrical potential Vs supply frequency at 4.5 kV.

FIG. 16. Power consumed by the device at 4.5kV/25kHz.

barrier discharges with unipolar pulse operation only rising and falling flank are used in the DBD discharge.[42]

Fig. 17 shows power consumed by the device at 3.5 kV and 6.5 kV applied voltages, respectively. It is observed from Fig. 17 that power consumed by the device increases from 0.12W at 10 kHz to 0.42 W at 25 kHz at the applied voltage 3.5 kV. A uniform discharge occurs all along the surface of the cathode and due to the increment in the frequency, the inherent collision process increases, which leads to better discharge condition indicated by single peak occurrence in the V-I characteristics of the developed APPJ. The relationship between power consumed by the device and supply frequency is shown in Fig. 17. The energy consumed per pulse (in joules) at 6.5 kV/25 kHz, (see Fig. 18) was found to be 4.24×10^{-5} J. This energy is multiplied with the supply frequency 25 kHz, which yields the power consumed by the device as 1.06 Joule/second or W. For combinations of higher supply voltages and frequency the power consumed by the device reaches a maximum value of 1.06 W at 6.5 kV, 25 kHz with the corresponding peak discharge current of 328 mA (see Fig. 18).Also, there is multiple streamer formation indicated by multiple peaks in Fig. 18. This rise of consumed power by the device is perhaps due to multiple steamer formation.[43–47] Hence it is established that there is a critical limit of supply voltage and frequency after which the input energy is not used for sustaining the plasma discharge. The
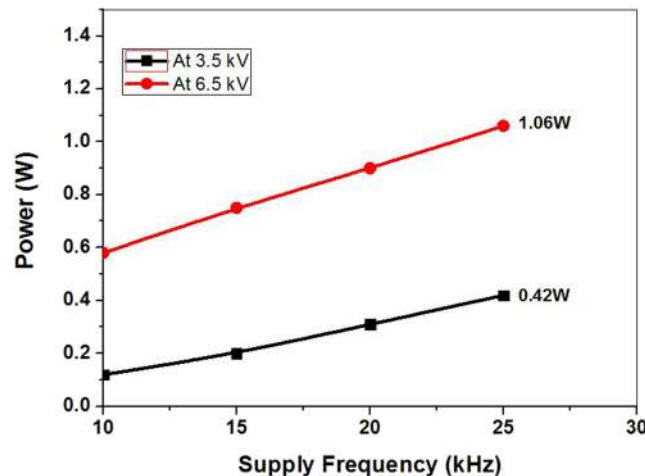

FIG. 17. Power consumed by the device Vs supply frequency at 3.5 & 6.5 kV.
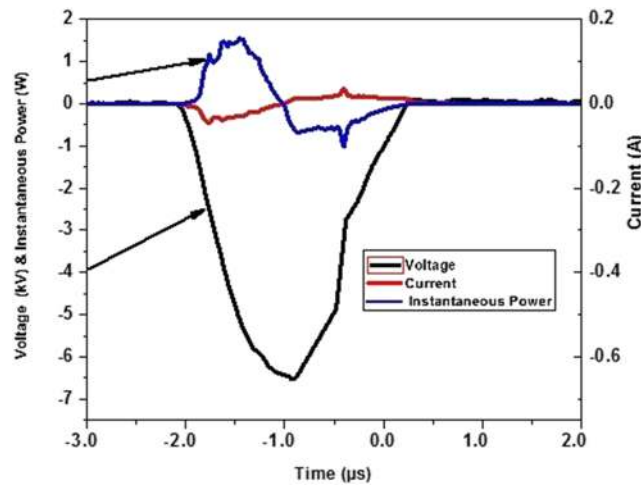
FIG. 18. Power consumed by the device 1.06W at 6.5kV/25kHz.

input energy is lost in the thermal dissipation to the dielectric material and that causes heating of quartz tube. This is indicated by the sudden rise in the power consumed by the device for higher voltages.

Fig. 19 illustrates the relationship between supply voltage and power consumed by the device. It is shown that at lower supply frequency and voltage (3.5kV/10kHz) power consumed by the device is less, as it is utilized for discharge initiation. However, at higher voltages (i.e., 5.5-6.5 kV) power consumed by the device increases from 0.35 W to 0.58 W as a result of more power being lost as heat in the thermal dissipation in the dielectric material leading to heating of the tube. However, it is intriguing to note that for the combinations of higher voltage and supply frequency, the power consumed by the device rises from 0.6 W (5.5 kV/25 kHz) to 1.06 W (6.5 kV, 25 kHz).

The most pivotal factor of the developed plasma jet, i.e., jet length is related to the supply frequency, voltage, and quartz sleeve. Jet length obtained at different supply voltages has been compared for both conditions of with and without the quartz sleeve. It is to be emphasized that a quartz sleeve is added on top of the nozzle of quartz tube to enhance the jet length by avoiding plasma jet interacting with surrounding air, which consists of electronegative gases and water vapor that impede the propagation of plasma jet. The jet length was measured 5 times for a particular combination of supply voltage and frequency. Further, error bars have been included in jet length
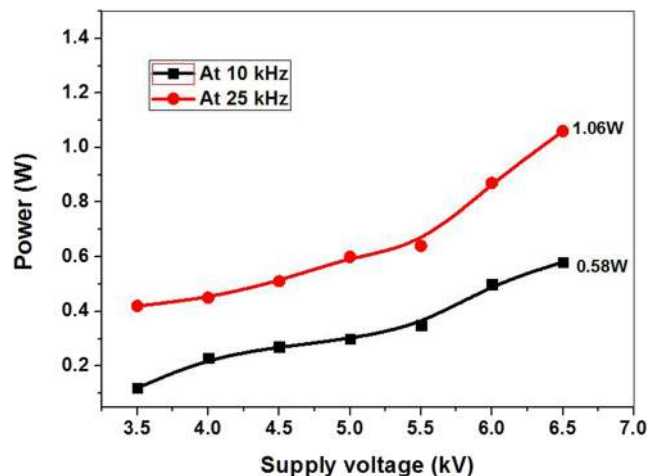

FIG. 19. Power consumed by the device Vs supply voltage at 10 kHz & 25 kHz.
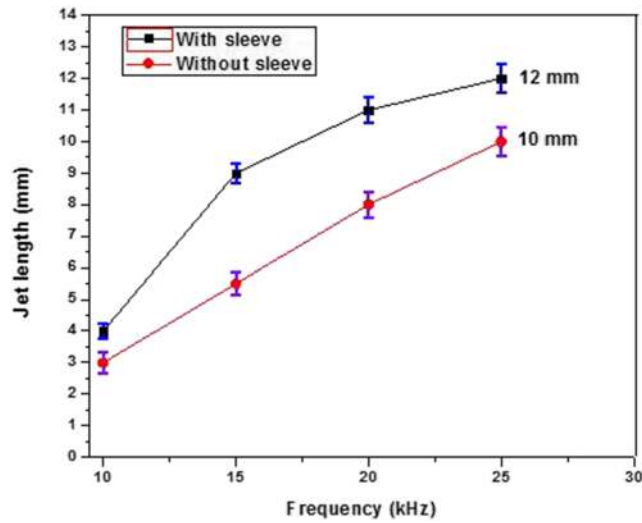
FIG. 20. Jet length Vs supply frequency at 4.5kV.

measurements as shown in Fig. 20 & Fig. 21. The uncertainty in the measured jet lengths is of the order of ± 0.5mm.

Jet length plays an imperative role in the application of these cold plasma jets in biomedical applications. Here the jet length is measured form the tip of the nozzle outlet as indicated in Fig. 2. The relationship between jet length and supply frequency is shown in Fig. 20 at 4.5 kV and in Fig. 21 at 6.5 kV, respectively. At low applied voltage, the jet length is shorter as the positive charges will be neutralized by the polarization charges induced in the region of the ground electrode thus limiting its propagation.[48–50] There is an increase in jet length at higher supply voltage and frequency due to already present energetic electrons that cause subsequent secondary ionization of argon atoms resulting in greater jet lengths. Hence as the supply voltage increases, more argon ions are created and their pronounced energy levels allow them to penetrate deeper into surrounding air leading to the formation of an extended jet (see Fig. 21). The maximum jet length reached at 6.5 kV/25 kHz with the sleeve is 26 mm, which is larger as compared to 20 mm (without sleeve) (see Fig. 21). The difference in jet length is due to the interaction of plasma jet with the surrounding air consisting of electronegative gases.
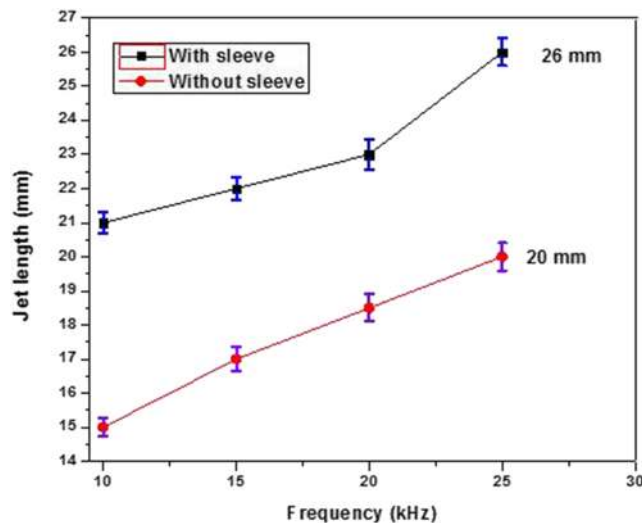

FIG. 21. Jet length Vs supply frequency at 6.5kV.

V. SUMMARY

Both simulation and experimental results of the developed dielectric barrier discharge based argon plasma jet in pin electrode configuration shows that the plasma parameters (i.e., electron density, electron temperature and electrical potential) increase with increase in supply frequency and supply voltage for both cases of static condition and with flow of argon gas. The maximum power consumed by the device for applied voltages (3.5-6.5 kV) has also been analyzed at supply frequencies (10-25 kHz). It has been experimentally found that that the maximum power consumed by the device is 1.06 W with corresponding peak discharge current of 328 mA at 6.5 kV/25 kHz, this fact is supported by the discharge simulation results, which shows highest electron density of $\sim 6.5 \times 10^{16}$ m^{-3} (Fig. 11) and electron temperature of 7.8 eV (Fig. 12) reached at the same applied conditions. At these operating parameters a fraction of the input power is lost in the thermal dissipation of the dielectric tube leading to its heating. It is established that for this kind of cold plasma jet generation the power consumed by the device and typical peak discharge current will be around 0.65 W and 212 mA-254 mA respectively, if the device is operated between optimum range of 4.5–5.5 kV and 15–25 kHz (see Fig. 17) for which the corresponding highest electron density and electron temperature reached are 4×10^{16} m^{-3} (Fig. 7) and 5.5 eV (Fig. 10). These values indicate that the device is being operated in glow discharge region without any arcing phenomenon which is imperative for a cold plasma jet to be used for various biomedical as well as technological applications. The effect of jet length enhancement is more at higher supply voltages. This is because electrons gain more energy resulting in more ionization and also expansion of luminous spots on the cathode occurs.[17]

The effect of quartz sleeve addition on the jet length has also been analyzed. A maximum jet length of 26 mm in pin electrode configuration was obtained with quartz sleeve compared to 20 mm without quartz sleeve. The difference in jet length is due to the interaction of plasma jet with the surrounding air consisting of electronegative gasses that impede the propagation of plasma jet. The practical applications of the developed pin electrode DBD with longer jet lengths and lower power operations may be realized for the direct plasma treatment on skin, however, this will require in vitro biomedical laboratory testing and study of biomedical changes and other sterilizing effects to establish the relevance. These cold plasma jets may also be employed in treatment of thermally sensitive materials.

ACKNOWLEDGMENTS

[1] P.-L. Girard-Lauriault, F. Mwale, M. Iordanova, C. Demers, P. Desjardins, and R. M. Wertheimer, Plasma Processes and Polymers **2**, 263 (2005).
[2] M. J. Shenton and G. C. Stevens, J. Phys. D: Appl. Phys. **34**, 2761 (2001).
[3] N. Abramzon, J. C. Joaquin, J. Bray, and G. Brelles-Mariño, IEEE Trans. Plasma Sci. **34**, 1304 (2006).
[4] M. Laroussi, IEEE Trans. Plasma Sci. **30**, 1409 (2002).
[5] O. Motret, O. Hibert, S. Pellerin, and J. M. Pouvesle, J. Phys. D: Appl. Phys. **1627** (2000).
[6] J. Woloszko, K. R. Stalder, and I. G. Brown, IEEE Trans. Plasma Sci. **30**, 235 (2002).
[7] W. Gorisch and K. P. Boergen, Lasers Surg. Med. **21**, 128 (1982).
[8] R. E. J. Sladek and E. Stoffels, J. Phys. D: Appl. Phys. **38**, 1716 (2005).
[9] V. I. Gibalov and G. J. Pietsch, J. Phys. D: Appl. Phys. **21**, 345 (2000).
[10] E. Stoffels, R. E. J. Sladek, I. E. Kieft, H. Kersten, and R. Wiese, Plasma Phys. Control. Fusion **46**, B167–B177 (2004).
[11] I. E. Kieft, J. L. V. Boers, V. Caubet-Hilloutou, D. W. Slaaf, and E. Stoffels, Bioelectromagnetics **25**, 362 (2004).
[12] I. E. Kieft, D. Darios, and E. Stoffels, IEEE Trans. Plasma Sci. **33**, 234 (2005).
[13] J. Park, I. Henins, H. W. Herrmann, G. S. Selwyn, and R. F. Hicks, J. Appl. Phys. **89**, 20 (2001).
[14] B. Eliasson and U. Kogelschatz, IEEE Trans. Plasma Sci. **19**, 1063 (1991).
[15] A. Schutze, J. Y. Jeong, S. E. Babayan, J. Park, G. S. Selwyn, and R. F. Hicks, IEEE Trans. Plasma Sci. **26**, 1685 (1998).
[16] M. A. Lieberman, *Principles of Plasma Discharges and Materials Processing* (Wiley, New York, 1994) p. 135
[17] Y. P. Raizer, *Gas Discharge Physics* (Springer-Verlag, Germany, 1991), p. 172.
[18] Liu and M. Neiger, J. Phys. D: Appl. Phys. **36**, 1632 (2003).
[19] M. Teschke, J. Kedzierski, E. G. Finantu-Dinu, D. Korzec, and J. Engemann, IEEE Transactions on Plasma Science **33**, 310 (2005).
[20] X. P. Lu and M. Laroussi, Journal of Applied Physics **100**, 063302 (2006).

[21] Y. C. Honga and H. S. Uhm, Applied Physics Letters **89**, 221504 (2006).
[22] X. P. Lu, Z. H. Jiang, Q. Xiong, Z. Y. Tang, X. W. Hu, and Y. Pan, Applied Physics Letters **92**, 081502 (2008).
[23] Q.-Y. Nie, C.-S. Ren, D.-Z. Wang, and J.-L. Zhang, Applied Physics Letters **93**, 011503 (2008).
[24] U. N. Pal, P. Gulati, N. Kumar, R. Prakash, and V. Srivastava, IEEE Trans. Plasma Sci. **40**, 1356 (2012).
[25] I. Radu, R. Bartnikas, G. Czeremuszkin, and M. R. Wertheimer, IEEE Trans. Plasma Sci. **31**, 411 (2003).
[26] H. Kim, A. Brockhaus, and J. Engemann, Applied Physics Letters **95**, 211501 (2009).
[27] H. Yi, L. Na, P. Jing, L. Jie, and W. Yan, Plasma Science and Technology **15**(8) (2013).
[28] H. M. Joh, H. R. Kang, T. H. Chung, and S. J. Kim, IEEE Trans. Plasma Sci. **42**, 3656 (2014).
[29] A. Shashurin and M. Keidar, Physics of Plasmas **22**, 122002 (2015).
[30] G. Divya Deepak, N. K. Joshi, U. Pal, and R. Prakash, Laser and Particle Beams **34**, 615 (2016).
[31] G. Divya Deepak, N. K. Joshi, D. Kumar Pal, and R. Prakash, Rev. Sci. Instrum. **88**, 013505 (2017).
[32] S. Kelly and M. Turner, in *fluid model of the 2D cross section of an AC driven plasma at atmospheric pressure 2011: Proceeding of 30th International Conference on Phenomenon in Ionized Gases*, National Centre for Plasma Science and Technology, Belfast UK, 28 August -2 September 2011, Topic number B5.
[33] C. Tendero, C. Tixier, P. Tristant, J. Desmaison, and P. Leprince, Spectraclinica Acta Part B: Atomic Spectroscopy **61**, 2 (2006).
[34] Y. Sakiyama and D. B. Graves, J. Phys. D: Appl. Phys. **39**, 3644 (2006).
[35] G. V. Naidis, J. Appl. Phys. **112**, 103304 (2012).
[36] S. Gadkari, X. Tu, and S. Gu, Physics of Plasmas **24**, 093509 (2017).
[37] G. J. M. Hagelaar and L. C. Pitchford, Plasma Sources Science and Technology **14**, 722 (2005).
[38] K. Van Laer and A. Bogaerts, Plasma Sources Sci. Technol. **25**(1), 015002 (2016).
[39] J. Reece Roth, *Industrial Plasma Engineering* vol.I (Institute of Physics, Bristol and Philadelphia, 1995) p. 117.
[40] Comsol Multiphysics, Sweden, https://www.kesco.co.jp/conference/2014/data/ConfTokyo2014Mini_Plasma_Module_General_Introduction.pdf, 2014 (accessed 9 March 2017).
[41] H. Yamada *et al.*, J. Phys. D: Appl. Phys. **49**, 394001.
[42] U. N. Pal, P. Gulati, R. Prakash, V. Srivastava, and S. Konar, Plasma Sci. Technol. **15**, 635 (2013).
[43] Z. Chen, G. Xia, Q. Zhou, Y. Hu, X. Zheng, Z. Zheng, L. Hong, P. Li, Y. Huang, and M. Liu, Rev. Sci. Instrum. **83**, 084701 (2012).
[44] Z. Chen, M. Liu, L. Hong, Q. Zhou, L. Cheng, and X. Hu, Phys. Plasmas **18**, 013505 (2011).
[45] Z. Chen, M. Liu, P. Zhou, W. Chen, C. Lan, and X. Hu, Plasma Sci. Technol. **10**, 655 (2008).
[46] T. J. Wu and C. S. Kou, Rev. Sci. Instrum. **70**, 2331 (1999).
[47] J. Munoz and M. D. Calzada, J. Phys. D **41**, 135203 (2008).
[48] R. B. Ye and W. Zheng, J. Phys. D **41**, 125202 (2008).
[49] R. B. Ye and W. Zheng, Appl. Phys. Lett. **93**, 071502 (2008).
[50] N. Jiang, A. Ji, and Z. Cao, J. Appl. Phys. **106**, 013308 (2009).